# Supporting Information

## Low-temperature processed additive-incorporated $CsPbIBr_2$-based inverted perovskite solar cell

Tuhin Ghosh and Debabrata Pradhan*

*Materials Science Centre, Indian Institute of Technology, Kharagpur 721 302, India*

*E-mail: deb@matsc.iitkgp.ac.in

**Characterization.** The crystallographic phase of the as-synthesized $CsPbIBr_2$ was analyzed by powder X-ray diffraction (PXRD) using Bruker D2 PHASER X-ray diffractometer (Cu Kα radiation, λ= 1.54 Å) in the 2θ range of 10–50°. The 2D XRD was performed using BRUKER D8 DISCOVER. The surface morphology of the as-synthesized materials was examined using field emission scanning electron microscope (FESEM) (MERLIN, Zeiss) operated at 5 kV. The thickness of different layers of solar device was examined by FESEM (Gemini 500, Zeiss) operated at 5 kV. The formation of highly crystalline structure of both with and without MACl incorporated $CsPbIBr_2$ were examined by transmission electron microscopy (TEM, TECNAI G2, FEI). The chemical composition and electronic structure of the as-deposited perovskite films was studied by X-ray photoelectron spectroscopy (XPS) with a PHI 5000 VersaProbe-II (ULVAC, PHI, Inc.) spectrometer, equipped with a micro-focused (100 μm, 25 W, 15 kV) monochromatic Al $K_\alpha$ X-ray source with an energy of 1486.6 eV. The topographical features of both without and with MACl-incorporated $CsPbIBr_2$ were examined by atomic force microscopy (AFM) (Agilent Technology, 5500). The optical absorbance and emission of the as-prepared samples was studied using UV-vis spectrophotometer (PerkinElmer Lambda 750) and photoluminescence spectrophotometer (PerkinElmer LS55), respectively. The time-resolved photoluminescence (TRPL) measurement was performed by time-correlated single

photon counting (TCSPC) spectrometer of IBH (U.K.). To characterize the PV performances and current–voltage (*J–V*) response of the fabricated devices, simulated AM 1.5 sunlight with a power intensity of 100 mW/cm$^2$ (Xenon Short Arc operated at 150 W using a Solar simulator, PHOTO EMISSION TECH., USA, SS50AAA) was used. The PV response, i.e., *J–V* curve of the solar device with an active device area and aperture area of of 0.1 cm$^2$, was recorded by a source meter (4200 SCS, Keithley) with a scan rate of 0.01 V/s. The external quantum efficiency (EQE) of the fabricated devices was measured using the Enlitech (QE-R) system. The impedance spectroscopic analysis was carried with a biopotentiostat (SP 150, BioLogic). The transient photocurrent (TPC) and transient photovoltage (TPV) were carried out in Metrohm AUTOLAB electrochemical analyzer. The glass rod used to form an active perovskite films has following dimension: length = 30 cm, radius = 0.25 cm, mass = 18.32 g, and weight = 0.18 N. It is to be noted that no additional force and/or power was used to prepare the perovskite thin film.

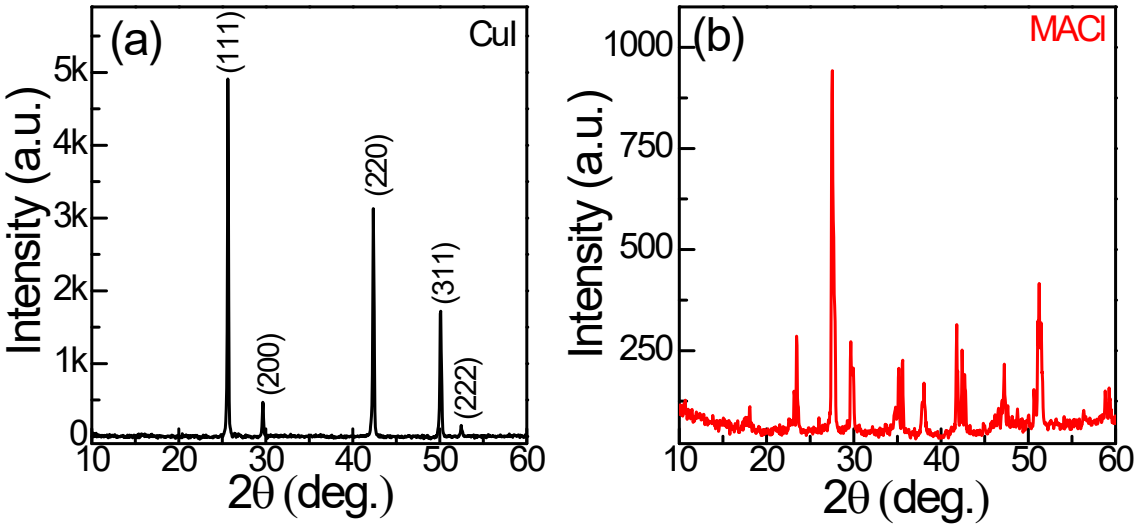


**Fig. S1.** XRD patterns of the as-synthesized (a) CuI and (b) MACl

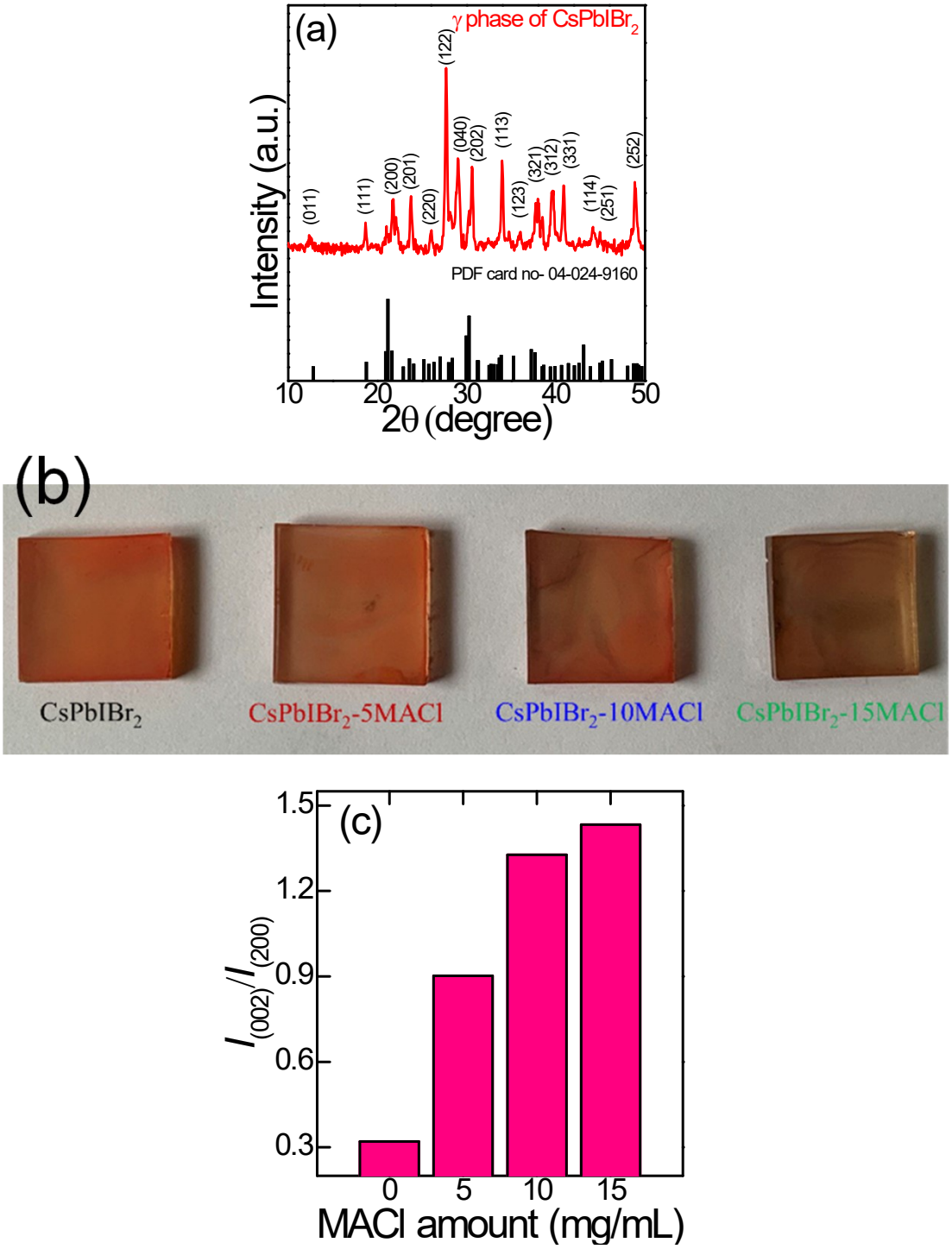


**Fig. S2.** (a) XRD pattern of the as-synthesized solid-state mixture of $CsPbIBr_2$ perovskite The orthorhombic (γ) phase of the as-synthesised $CsPbIBr_2$ perovskite powder matches well with the JCPDS card No. 04-024-9160, (b) photographs and (c) (002)/(200) direction intensity of $CsPbIBr_2$ and MACl-incorporated $CsPbIBr_2$ thin films.

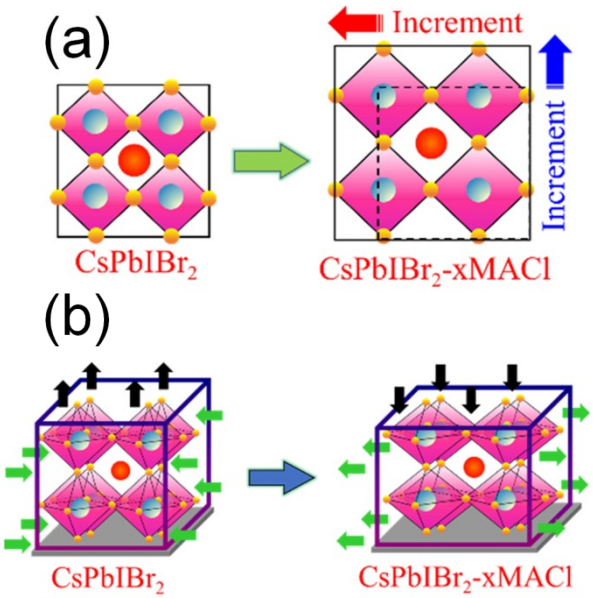


**Fig. S3.** (a) Schematic representation of the lattice expansion and (b) conversion of lattice strain from compressive to tensile due to MACl incorporation within $CsPbIBr_2$

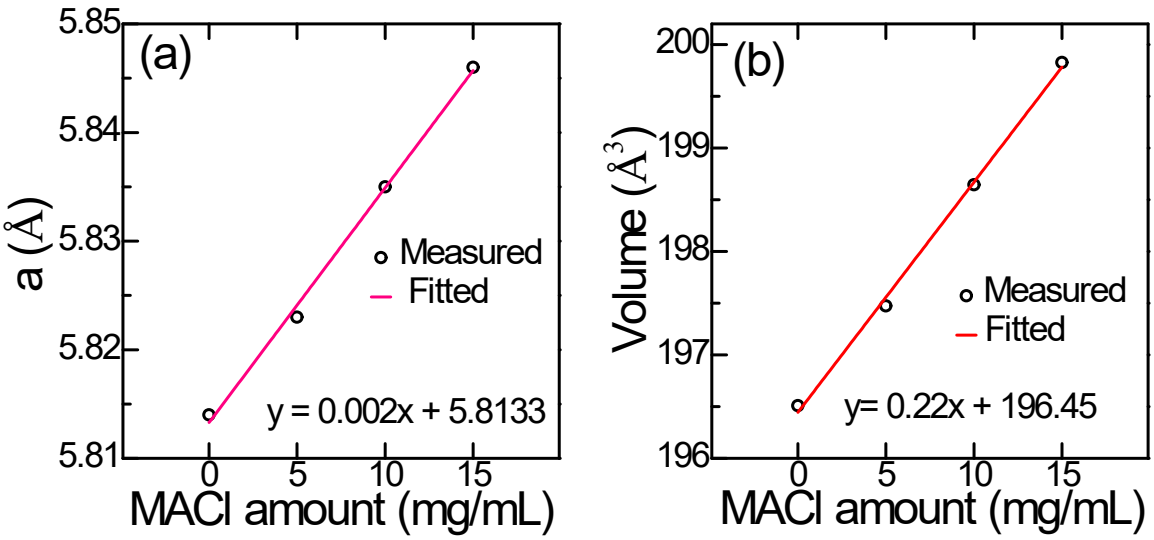


**Fig. S4.** Fitting plot of (a) lattice parameter and (b) crystal volume of without and with MACl-incorporated $CsPbIBr_2$ films

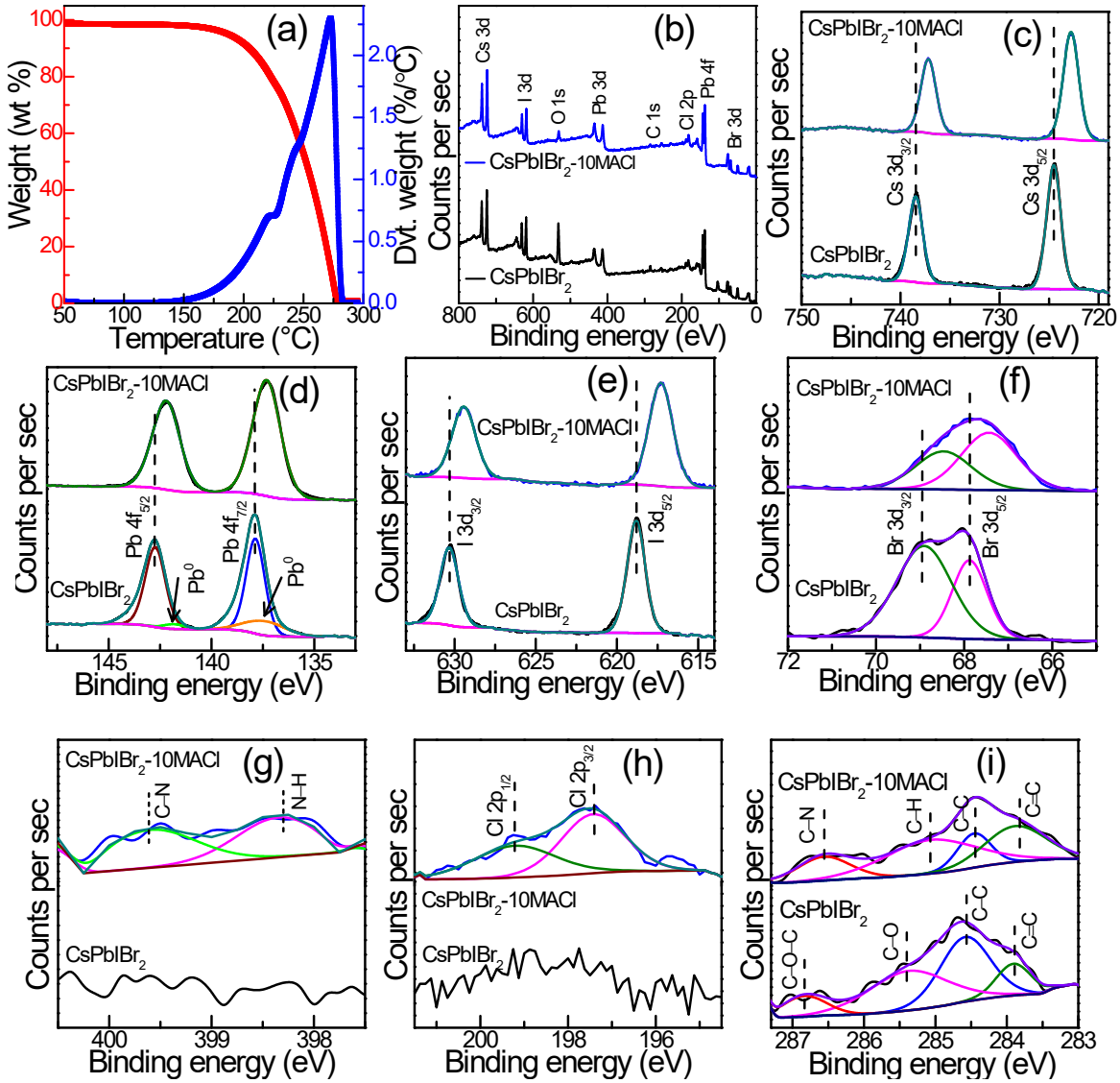


**Fig. S5.** (a) TGA plot of MACl, and (b) XPS survey, (c) Cs 3d, (d) Pb 4f, (e) I 3d, (f) Br 3d, (g) N 1s, (h) Cl 2p and (i) C 1s spectra of $CsPbIBr_2$-10MACl and $CsPbIBr_2$

**Table S1.** The percentage of C–N and C=N bonding using N 1s region spectra (Fig. S6g)

| *Active layer* | C–N (%) | N–H (%) |
|---|---|---|
| $CsPbIBr_2$ | Absent | Absent |
| $CsPbIBr_2$-10MACl | 48.46 | 51.54 |

**Table S2.** The carbon atomic percentages with different bonding using XPS analysis (Fig. S5i)

| *Active layer* | C=C | C–C | C–O–C | C–O | C–H | C–N |
|---|---|---|---|---|---|---|
| $CsPbIBr_2$ | 13.16 | 38.75 | 10.85 | 37.25 | Absent | Absent |
| $CsPbIBr_2$-10MACl | 42.96 | 6.37 | Absent | Absent | 33.39 | 17.28 |

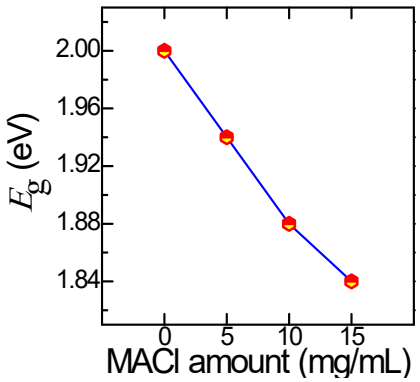


**Fig. S6.** Band gap variation of $CsPbIBr_2$ and $CsPbIBr_2$-xMACl perovskite layer

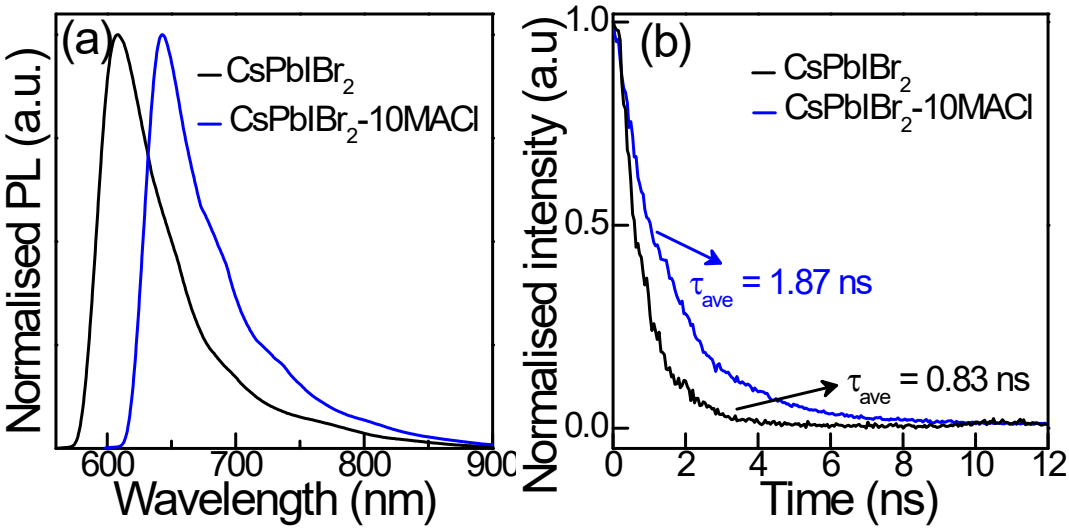


**Fig. S7.** (a) PL and (b) TRPL variation of $CsPbIBr_2$ and $CsPbIBr_2$-10MACl perovskite layer

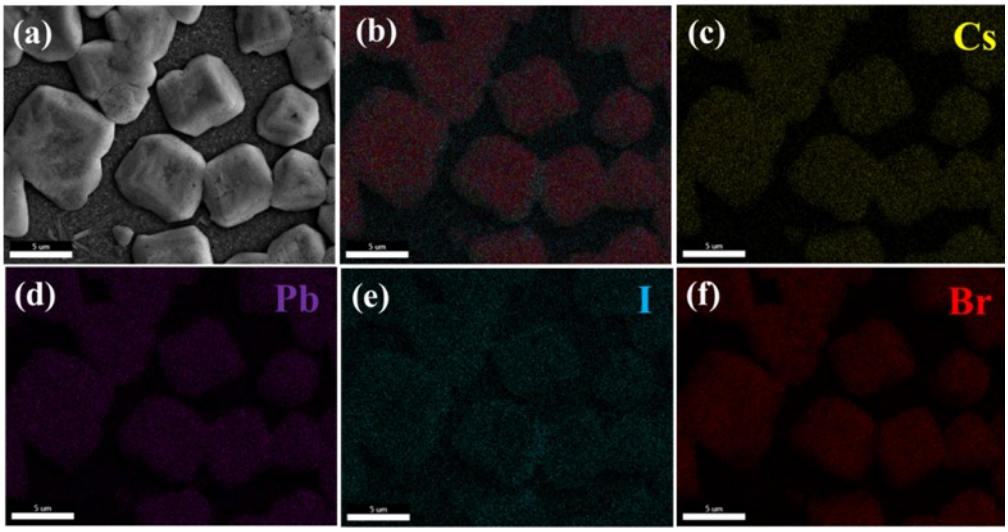


**Fig. S8.** (a) SEM image of $CsPbIBr_2$ film and corresponding EDX elemental mapping, (b) overlapped EDX signal of all elements shown in (c) Cs, (d) Pb, (e) I, and (f) Br in the $CsPbIBr_2$ film.

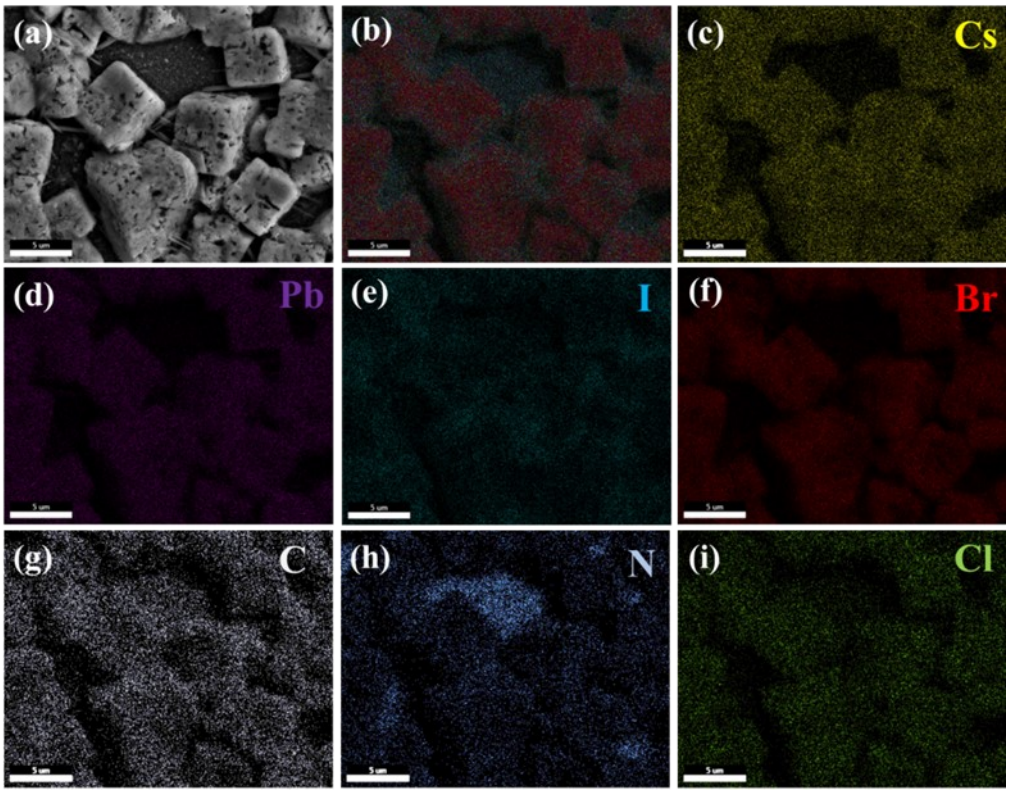


**Fig. S9.** (a) SEM image of $CsPbIBr_2$-10MACl film and corresponding EDX elemental mapping, (b) overlapped EDX signals of all elements shown in (c) Cs, (d) Pb, (e) I, (f) Br, (g) C, (h) N, and (i) Cl in the $CsPbIBr_2$-10MACl film.

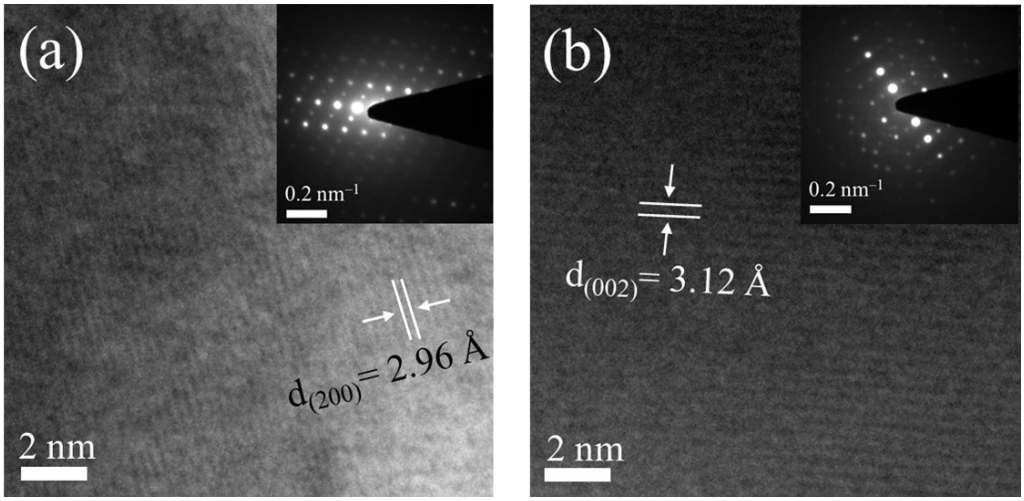


**Fig. S10.** TEM analysis of (a) $CsPbIBr_2$ and (b) $CsPbIBr_2$-10MACl with measured inter planar spacing.

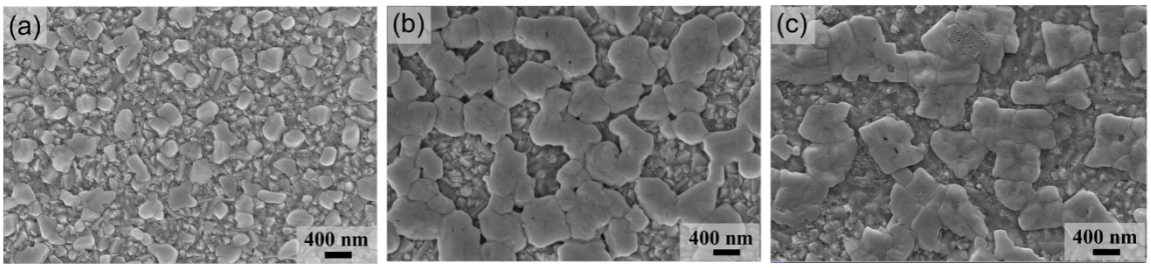


**Fig. S11.** FESEM images of the perovskite thin films obtained by varying the annealing time (a) 15 min, (b) 30 min, and (c) 45 min.

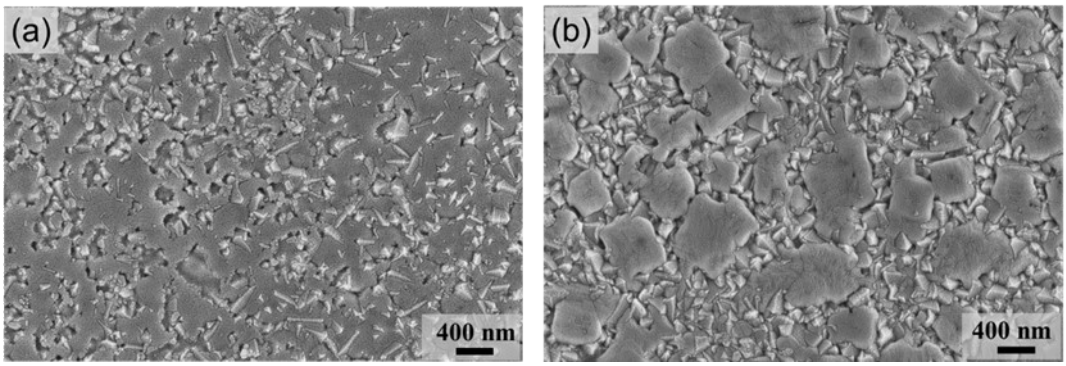


**Figure S12.** FESEM images of (a) $CsPbIBr_2$ and (b) $CsPbIBr_2$-10MACl perovskite thin films obtained by spin coating method.

**Table S3.** Photophysical properties of PSC devices with active layer, i.e., $CsPbIBr_2$ and $CsPbIBr_2$-10MACl.

| *$CsPbIBr_2$ based Cells* | *$V_{OC}$ (V)* | *$J_{SC}$ (mA/cm$^2$)* | *FF* | *PCE (%)* | *$CsPbIBr_2$-10MACl based Cells* | *$V_{OC}$ (V)* | *$J_{SC}$ (mA/cm$^2$)* | *FF* | *PCE (%)* |
|---|---|---|---|---|---|---|---|---|---|
| 1 | 0.9 | 11.40 | 0.511 | 5.24 | 1 | 1.16 | 12.06 | 0.586 | 8.20 |
| 2 | 0.89 | 10.96 | 0.499 | 4.87 | 2 | 1.14 | 11.70 | 0.580 | 7.73 |
| 3 | 0.79 | 10.53 | 0.508 | 4.22 | 3 | 1.15 | 11.98 | 0.584 | 8.04 |
| 4 | 0.85 | 11.01 | 0.501 | 4.69 | 4 | 1.14 | 12.08 | 0.579 | 7.97 |
| 5 | 0.91 | 11.35 | 0.498 | 5.14 | 5 | 1.13 | 12.06 | 0.585 | 7.97 |
| 6 | 0.84 | 11.28 | 0.502 | 4.75 | 6 | 1.15 | 12.00 | 0.585 | 8.07 |
| 7 | 0.89 | 11.3 | 0.489 | 4.92 | 7 | 1.13 | 11.76 | 0.581 | 7.72 |
| 8 | 0.87 | 11.35 | 0.495 | 4.89 | 8 | 1.1 | 12.48 | 0.582 | 7.99 |
| 9 | 0.84 | 10.88 | 0.496 | 4.53 | 9 | 1.14 | 11.68 | 0.563 | 7.49 |
| 10 | 0.78 | 11.18 | 0.502 | 4.38 | 10 | 1.17 | 11.93 | 0.565 | 7.89 |
| 11 | 0.86 | 11.38 | 0.511 | 5.00 | 11 | 1.18 | 11.71 | 0.584 | 8.07 |
| 12 | 0.89 | 11.10 | 0.49 | 4.84 | 12 | 1.11 | 11.71 | 0.584 | 7.59 |
| 13 | 0.84 | 11.03 | 0.505 | 4.68 | 13 | 1.15 | 11.98 | 0.570 | 7.86 |
| 14 | 0.86 | 10.97 | 0.46 | 4.34 | 14 | 1.09 | 12.01 | 0.585 | 7.66 |
| 15 | 0.86 | 11.29 | 0.504 | 4.90 | 15 | 1.11 | 11.87 | 0.580 | 7.65 |
| 16 | 0.88 | 11.25 | 0.516 | 5.11 | 16 | 1.11 | 11.70 | 0.576 | 7.48 |
| 17 | 0.83 | 10.98 | 0.483 | 4.40 | 17 | 1.09 | 11.82 | 0.579 | 7.47 |
| 18 | 0.85 | 11.39 | 0.493 | 4.77 | 18 | 1.15 | 10.96 | 0.585 | 7.37 |
| 19 | 0.89 | 11.38 | 0.497 | 5.03 | 19 | 1.13 | 11.90 | 0.581 | 7.82 |
| 20 | 0.82 | 11.29 | 0.461 | 4.28 | 20 | 1.14 | 11.98 | 0.585 | 7.99 |

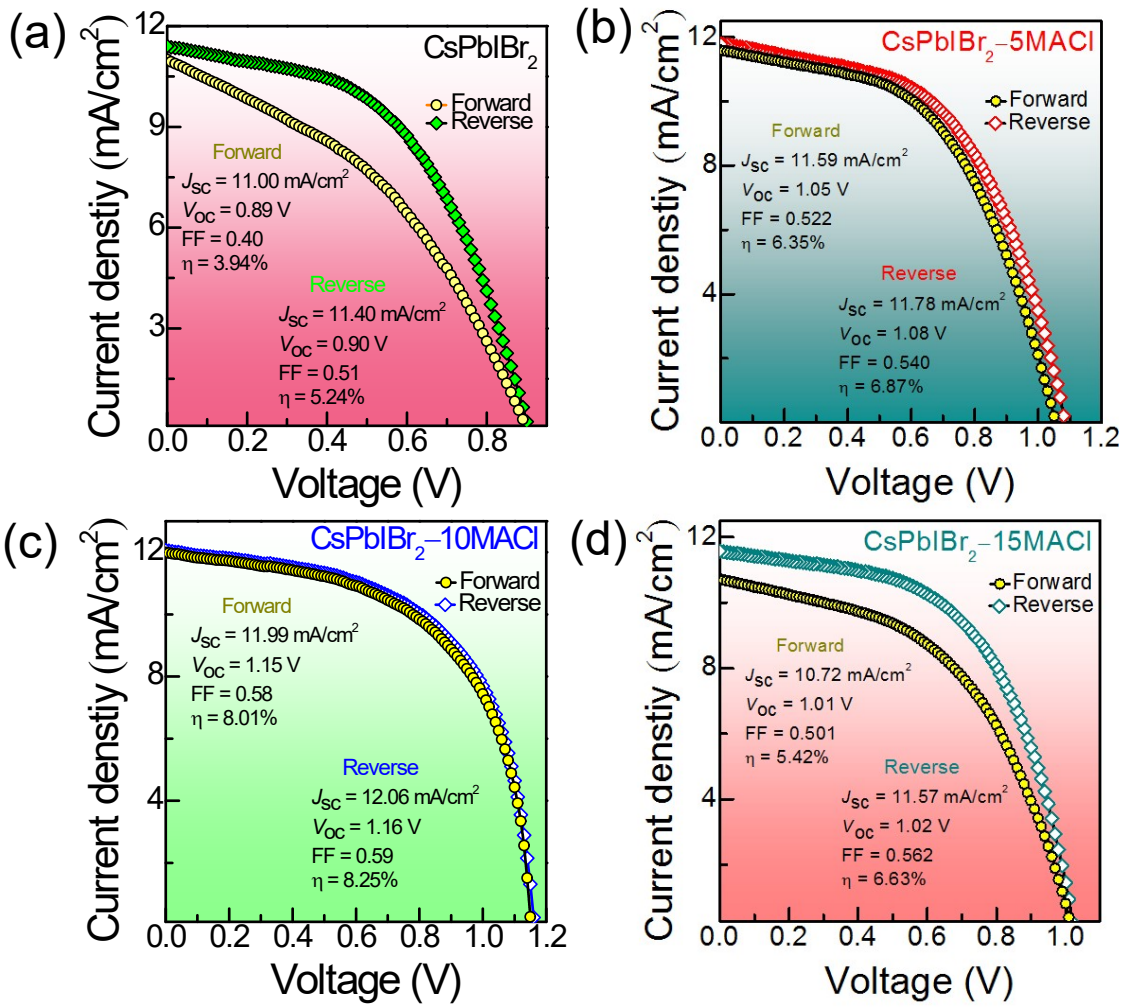


**Fig. S13.** *J–V* curves of the (a) $CsPbIBr_2$, (b) $CsPbIBr_2$–5MACl, (c) $CsPbIBr_2$–10MACl ,and (d) $CsPbIBr_2$–15MACl-based PSC with both scan directions

**Table S4.** PV performances of the present fabricated PSC with the other $CsPbIBr_2$ based PSCs as reported in literature.

| *Sl No.* | *Device architecture* | *$J_{SC}$ (mA/cm$^2$)* | *$V_{OC}$ (V)* | *PCE (%)* | *Temp. (℃)* | *Ref.* |
|---|---|---|---|---|---|---|
| 1. | FTO/CuI/$CsPbIBr_2$/Al | 11.40 | 0.90 | 5.24 | 110 | This work |
| 2. | FTO/CuI/$CsPbIBr_2$-10MACl/Al | 12.06 | 1.16 | 8.25 | 110 | This work |
| 3. | FTO/$TiO_2$/$CsPbIBr_2$-10MACl/PEDOT:PSS/Au | 12.89 | 1.26 | 10.18 | 110 | This Work |
| 4. | FTO/c-$TiO_2$/$CsPbIBr_2$/Carbon | 10.66 | 1.24 | 9.16 | 280 | 1 |
| 5. | FTO/$NiO_x$/$CsPbIBr_2$/$MoO_x$/Au | 10.56 | 0.85 | 5.52 | 160 | 2 |
| 6. | FTO/c-$TiO_2$/$CsPbIBr_2$/ Spiro-OMeTAD /Au | 9.69 | 1.22 | 8.02 | 320 | 3 |
| 7. | FTO/c-$TiO_2$/m-$TiO_2$/$CsPbIBr_2$/ Spiro-OMeTAD /Au | 7.8 | 1.12 | 6.30 | 300 | 4 |
| 8. | FTO/c-$TiO_2$/$CsPbIBr_2$/Au | 8.7 | 0.921 | 4.70 | 250 | 5 |
| 9. | FTO/$SnO_2$/C60/$CsPbIBr_2$/Spiro-OMeTAD/Au | 8.32 | 1.18 | 7.34 | 150 | 6 |
| 10. | ITO/ZnO/$CsPbIBr_2$/ Spiro-OMeTAD/Ag | 11.52 | 1.27 | 10.16 | 160 | 7 |
| 11. | ITO/$SnO_2$/$CsPbIBr_2$/Carbon | 8.50 | 1.23 | 7.00 | 180 | 8 |
| 12. | FTO/$In_2S_3$/$CsPbIBr_2$/Spiro-OMeTAD /Ag | 7.76 | 1.09 | 5.59 | 160 | 9 |
| 13. | FTO/c-$TiO_2$/$CsPbIBr_2$(GuaSCN 3%)/Spiro-OMeTAD/Au | 10.90 | 1.23 | 12.05 | 280 | 10 |
| 14. | FTO/c-$TiO_2$/$CsPbIBr_2$(BAI0.1%)/Spiro-OMeTAD/Au | 10.78 | 1.25 | 11.63 | 160 | 11 |
| 15. | FTO/$TiO_2$/PEG-$CsPbIBr_2$/Spiro-OMeTAD/Ag | 11.10 | 1.21 | 12.25 | 200 | 12 |

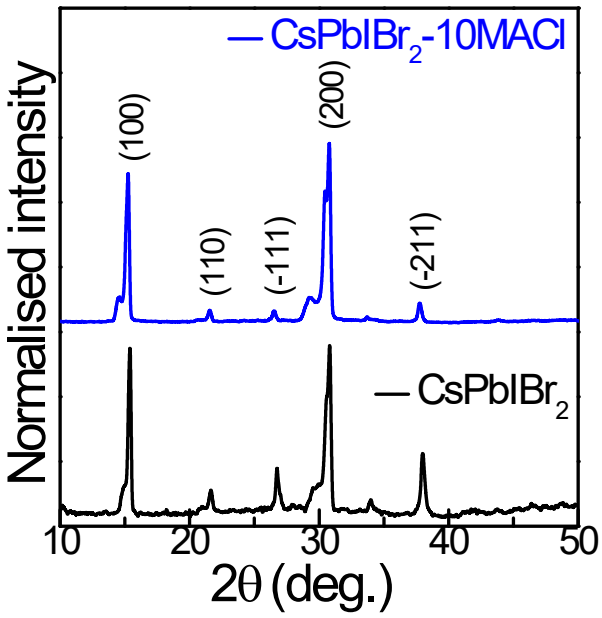


**Fig. S14.** XRD patterns of $CsPbIBr_2$ and $CsPbIBr_2$-10MACl film after 3 months of preparation.

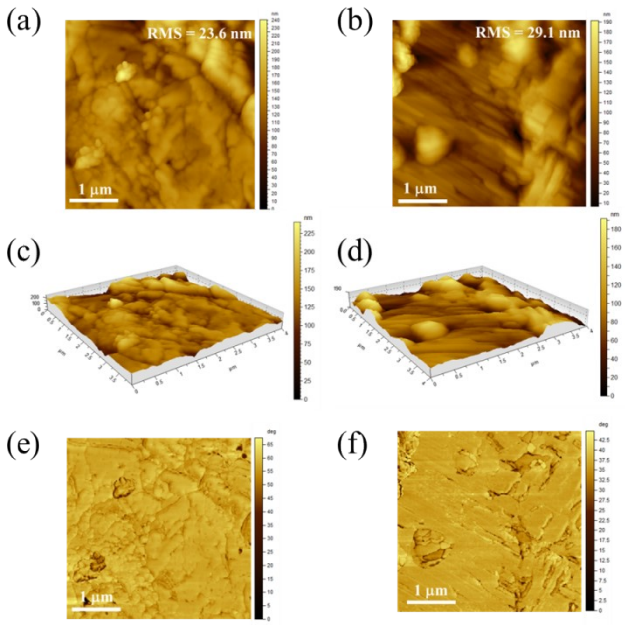


**Fig. S15.** AFM analysis of (a, c and e) $CsPbIBr_2$-10MACl and (b, d and f) $CsPbIBr_2$.

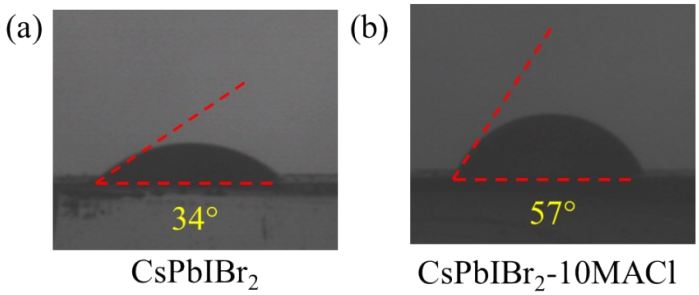


**Fig. S16.** Contact angle measurements of (a) $CsPbIBr_2$ and $CsPbIBr_2$-10MACl.

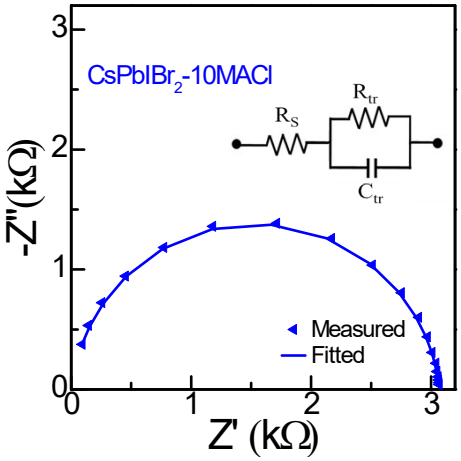


**Fig. S17.** Fitted Nyquist plot of $CsPbIBr_2$–xMACl and inset shows the fitted circuit diagram.

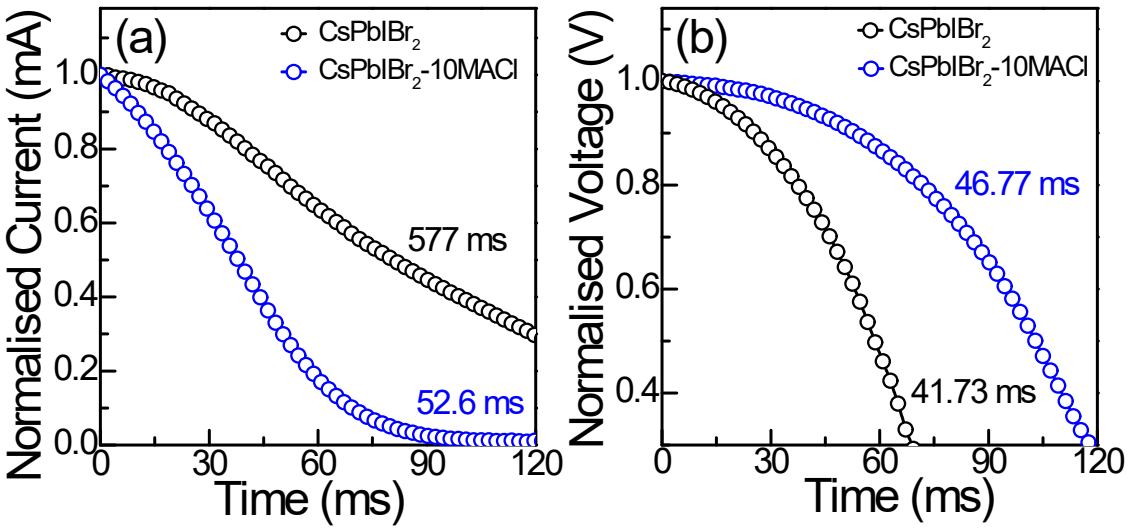


**Fig. S18.** (a) TPC and (b) TPV measurements of $CsPbIBr_2$-10MACl and $CsPbIBr_2$.

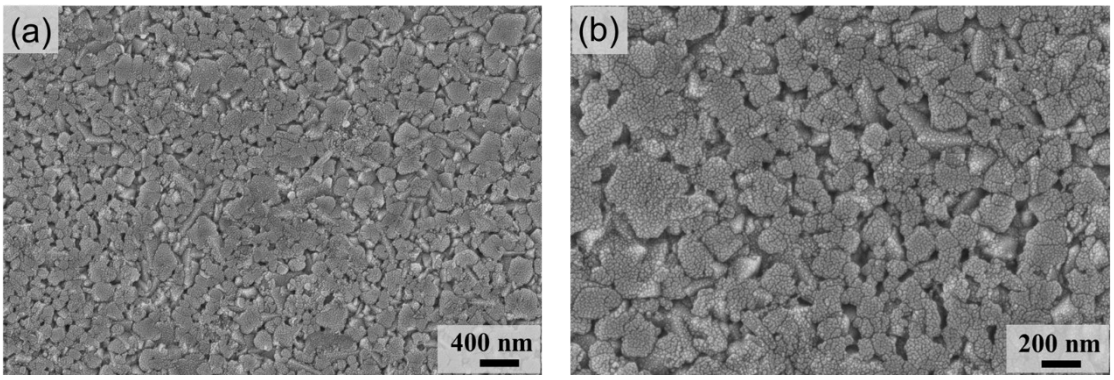


**Fig. S19.** (a,b) FESEM images of $CsPbIBr_2$ thin film obtained using salt precursors.

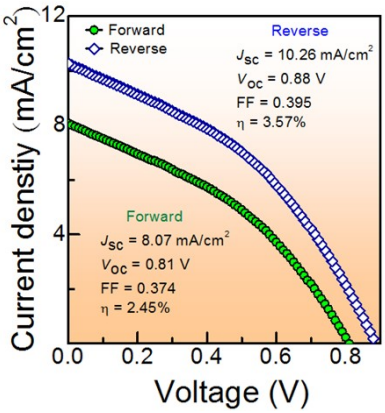


**Fig. S20.** *J–V* curves of the device fabricated with $CsPbIBr_2$ thin film prepared using salt precursors.

## References


[1] Zhu, W.; Zhang, Q.; Chen, D.; Zhang, Z.; Lin, Z.; Chang, J.; Zhang, J.; Zhang, C.; Hao, Y. Intermolecular Exchange Boosts Efficiency of Air-Stable, Carbon-Based All-Inorganic Planar $CsPbIBr_2$ Perovskite Solar Cells to Over 9%. *Adv. Energy Mater.* **2018**, *8*, 1802080.

[2] Liu, C.; Li, W.; Chen, J.; Fan, J.; Mai, Y.; Schropp, R. E. I. Ultra-Thin MoOx as Cathode Buffer Layer for the Improvement of All-Inorganic $CsPbIBr_2$ Perovskite Solar Cells. *Nano Energy* **2017**, *41*, 75–83.

[3] Li, W.; Rothmann, M. U.; Liu, A.; Wang, Z.; Zhang, Y.; Pascoe, A. R.; Lu, J.; Jiang, L.; Chen, Y.; Huang, F.; et al. Phase Segregation Enhanced Ion Movement in Efficient Inorganic $CsPbIBr_2$ Solar Cells. *Adv. Energy Mater.* **2017**, *7*, 1700946.

[4] Lau, C. F. J.; Deng, X.; Ma, Q.; Zheng, J.; Yun, J. S.; Green, M. A.; Huang, S.; Ho-Baillie, A. W. Y. $CsPbIBr_2$ Perovskite Solar Cell by Spray-Assisted Deposition. *ACS Energy Lett.* **2016**, *1*, 573–577.

[5] Ma, Q.; Huang, S.; Wen, X.; Green, M. A.; Ho-Baillie, A. W. Y. Hole Transport Layer Free Inorganic $CsPbIBr_2$ Perovskite Solar Cell by Dual Source Thermal Evaporation. *Adv. Energy Mater.* **2016**, *6*, 1502202.

[6] Li, N.; Zhu, Z.; Li, J.; Jen, A. K.-Y.; Wang, L. Inorganic $CsPb_{1-x}Sn_xIBr_2$ for Efficient Wide-Bandgap Perovskite Solar Cells. *Adv. Energy Mater.* **2018**, *8*, 1800525.

[7] Wang, H., Cao, S., Yang, B., Li, H., Wang, M., Hu, X., Sun, K. and Zang, Z. $NH_4Cl$-Modified ZnO for High-Performance $CsPbIBr_2$ Perovskite Solar Cells via Low-Temperature Process. *Sol. RRL* **2020**, *4*, 1900363.

[8] Guo, Z.; Teo, S.; Xu, Z.; Zhang, C.; Kamata, Y.; Hayase, S.; Ma, T. Achievable High V Oc of Carbon Based All-Inorganic CsPbIBr 2 Perovskite Solar Cells through Interface Engineering. *J. Mater. Chem. A* **2019**, *7*, 1227–1232.

[9] Yang, B.; Wang, M.; Hu, X.; Zhou, T.; Zang, Z. Highly Efficient Semitransparent $CsPbIBr_2$ Perovskite Solar Cells via Low-Temperature Processed $In_2S_3$ as Electron-Transport-Layer. *Nano Energy* **2019**, *57*, 718–727.

[10] Wang, Q.; Xu, Y.; Zhang, L.; Yang, A.; Bai, T.; Liu, F.; Lyu, M.; Zhu, J. Guanidinium Thiocyanate Additive Engineering for High-Performance $CsPbIBr_2$ Solar Cells with an Efficiency of 10.90%, *ACS Appl. Energy Mater.* **2022**, *5*, 3110–3118.

[11] You, Y.; Tian, W.; Wang, M.; Cao, F.; Sun, H.; Li, L. PEG Modified $CsPbIBr_2$ Perovskite Film for Efficient and Stable Solar Cells, *Adv. Mater. Interfaces* **2020**, *7*, 2000537.

[12] Y. You, W. Tian, M. Wang, F. Cao, H. Sun and L. Li, PEG Modified $CsPbIBr_2$ Perovskite Film for Efficient and Stable Solar Cells, *Adv. Mater. Interfaces*, 2020, **7**, 2000537.